Dynamic Response Evaluation of Damped-Outrigger Systems with Various Heights

Bin Huang[a] **and Toru Takeuchi**[a]

Outriggers are a proven and effective system used to reduce the dynamic response of tall buildings. By inserting dampers into the outriggers, providing supplementary energy dissipation, further improvements in the dynamic response can be achieved. The aim of this study is to develop analytical methods for the dynamic response evaluation of a single-damped-outrigger system and determine the optimal outrigger locations and damper sizes to minimize response. Changes in the mode shape, damping, natural period and seismic response were studied parametrically using complex eigenvalue analysis of a continuous cantilever model, and the accuracy verified by comparison with a member-by-member model. A simplified single-degree-of-freedom model was then constructed and studied using an assumed lateral displacement curve and the principle of virtual work. Finally, a practical method for determining optimal outrigger location and damper size based on this simplified model was proposed. [DOI: 10.1193/051816EQS082M]

INTRODUCTION

Outriggers are widely used around the world in many high-rise building structures (Lu et al. 2007, Ali et al. 2007). Traditionally, an outrigger is introduced to rigidly connect the core to a perimeter frame, improving the lateral stiffness of the overall structural system and reducing the dynamic response. However, it has been pointed out that it is difficult to design and detail conventional outrigger due to local stress concentrations at the outrigger-structure connection, and consequently the cost of the outrigger floor is high (Viise et al. 2014).

An efficient approach to overcome this difficulty is to use damping rather than stiffness to mitigate the dynamic response, replacing the rigid outrigger connection with supplementary energy-dissipation devices. This is called the damped-outrigger system. A 60-story twin tower structure in Manila employing an outrigger with fluid-viscous dampers was completed in 2009, demonstrating the effectiveness of dampers in reducing the overturning moment, base shear and accelerations resulting from dynamic actions (Willford et al. 2008, Smith et al. 2007). Analytical, numerical, and experimental studies have also been conducted to demonstrate the damped-outrigger's seismic response reducing capacity (Tan et al. 2012). However, practical methods for finding the optimal damped-outrigger location and damper size has been limited to manual trial and error or brute force approaches, which lack a theoretical basis and are less efficient than a direct analytical method.

[a] Department of Architecture and Building Engineering, Tokyo Institute of Technology, Tokyo, Japan

Earthquake Spectra, Volume 33, No. 2, pages 665–685, May 2017; © 2017, Earthquake Engineering Research Institute

Previous attempts have been made to develop an analytical model capable of accurately estimating the damping of the single-damped-outrigger system, but these have not been validated against a range of building heights and are too complex for practical use. Chen et al. (2010) obtained the complex mode shapes and eigenvalues for a continuous cantilever beam with a damped outrigger by solving the free vibration partial differential equation of motion, and proposed a method to approximately determine the optimal first-mode damping ratio and damper size (Chen et al. 2010). Tan et al. (2014) used the dynamic stiffness method to investigate the effect of damper size and outrigger location on the mode damping ratio. Other approaches to evaluate mode damping based on the principle of virtual work have also been applied (Chen et al. 2009, Jeremiah 2006). Further relevant studies using the continuous cantilever model can be found in beam vibration control theory from the applied mechanics field (Wu et al. 1998, 1999; Laura et al. 1977). These methods require validation against a range of building heights and further simplification to be of practical use.

This paper develops a complex eigenvalue analysis (CEA) method to obtain complex mode shapes, damping ratios and periods for three single-damped-outrigger models with varying heights, taking into account higher modes. This method is validated by comparing the seismic response, including peak lateral displacement and story drift, to corresponding member-by-member (MBM) models. Following a parametric study using this CEA method, a simplified single-degree-of-freedom (SDOF) method is proposed to approximately evaluate the dynamic response of the single-damped-outrigger system, and determine the optimal outrigger location and damper size. The proposed optimal design method is supposed to be able to help avoid trial-and-error studies in conventional outrigger design process.

COMPLEX EIGENVALUE ANALYSIS

The damped-outrigger system can be simplified as a continuous cantilever (RC core) with a nonlinear rotational spring (damped-outrigger plus perimeter columns) at the outrigger floor, as shown in Figure 1. The bending stiffness of beams and slabs on non-outrigger floors is neglected.

In this figure, MBM refers to a member-by-member stick model constructed in OpenSees (Mazzoni et al. 2009) and used for validation, and CEA refers to complex eigenvalue analysis of an equivalent continuous cantilever model. k_t is the lateral stiffness of an outrigger truss, l_t is the length of an outrigger truss, k_c is the axial stiffness of column, c_d is the damping coefficient (damper size), EI_c is the bending stiffness of the RC core, m_c is the distributed mass along the RC core, k_r is the equivalent rotational stiffness of the cantilever truss, damper and perimeter columns, and $y(x,t)$ is the physical lateral deformation curve of the building. The total height of the building is h, and the outrigger is located at αh.

The free vibration equation of motion for a continuous cantilever with a concentrated rotational spring at the outrigger floor is given by Equation 1, with the origin point taken as the floor where the outrigger is located:

$$EI_c \frac{\partial^4 y(x,t)}{\partial x^4} + m_c \frac{\partial^2 y(x,t)}{\partial t^2} + \frac{\partial q(x,t)}{\partial x} = 0, \quad q(x,t) = -\frac{\partial y(x,t)}{\partial x} k_r \delta(x) \tag{1}$$

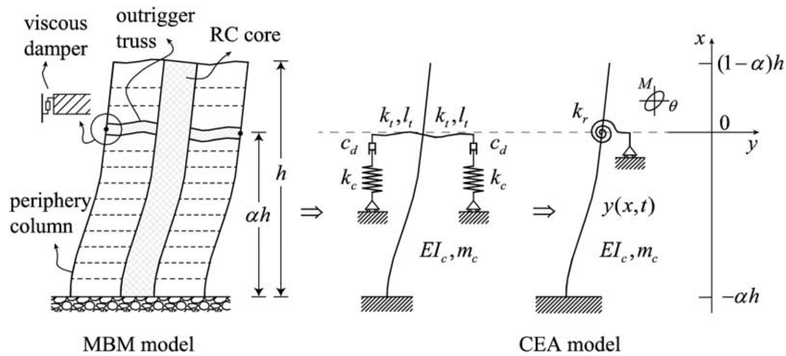

Figure 1. Damped-outrigger continuous cantilever model.

where $q(x,t)$ stands for the resisting moment contribution of the column, damper and outrigger truss, and $\delta(x)$ $(= +\infty \text{ for } x = 0, 0 \text{ for } x \neq 0)$ is the Dirac delta function. Also, k_r is given by Equation 2 (online Appendix A):

$$k_r = \frac{2k_b l_t^2 \omega c_d i}{k_b + \omega c_d i}, \quad k_b^{-1} = k_t^{-1} + \left(\frac{k_c}{\alpha}\right)^{-1} \tag{2}$$

Represents the rotation stiffness of the nonlinear rotational spring as shown in Figure 1, and ω is the circular frequency. The physical lateral deformation curve has the form of $y(x,t) = Y(x)e^{i\omega t}$, with normalized values $\bar{Y}(\bar{x}) = Y(x)/h$ and $\bar{x} = x/h$ introduced for mathematical convenience. Equation 1 results in an ordinary differential equation with the general solution (Appendix B):

$$\begin{aligned}\bar{Y} = {} & C_1 \frac{1}{\lambda} e^{\lambda \bar{x}} + C_2 \cos \lambda \bar{x} + C_3 (e^{-\lambda \bar{x}} + e^{\lambda \bar{x}}) \\ & + C_4 (\sin \lambda \bar{x} - e^{\lambda \bar{x}}) + C_1 c (\cosh \lambda \bar{x} - \cos \lambda \bar{x}) H(\bar{x})\end{aligned} \tag{3}$$

The Heaviside step function, $H(\bar{x})$, is used to describe the different lateral displacement curves below and above the outrigger. The boundary conditions for Equation 3 are taken as:

$$\bar{Y}(-\alpha) = 0, \quad \bar{Y}'(-\alpha) = 0, \quad \bar{Y}''(1-\alpha) = 0, \quad \bar{Y}^{(3)}(1-\alpha) = 0 \tag{4}$$

Substituting Equation 3 into Equation 4, the boundary condition matrix is obtained by:

$$[Bou.]\{C\} = 0, \quad \{C\} = \{C_1, C_2, C_3, C_4\}^T \tag{5}$$

Using the nontrivial solution condition $\det(Bou.) = 0$, one finally gets the transcendental equation containing the complex eigenvalue λ with $\lambda \neq 0$:

$$\begin{aligned} & c\lambda[2\cosh(\alpha\lambda)\cdot\cosh(\lambda-\alpha\lambda)\cdot\sin\lambda \\ & \quad + 2\cosh(\alpha\lambda)\sin(\alpha\lambda) - 2\cosh(\lambda-\alpha\lambda)\sin(\lambda-\alpha\lambda) \\ & \quad + \cos\lambda\sinh\lambda + \cos(\lambda-2\alpha\lambda)\sinh\lambda \\ & \quad + 2\cos(\alpha\lambda)\sinh(\alpha\lambda) - 2\cos(\lambda-\alpha\lambda)\sinh(\lambda-\alpha\lambda)] \\ & \quad + 2(\cos\lambda\cosh\lambda + 1) = 0 \end{aligned} \tag{6}$$

where:

$$\lambda^4 = \frac{m_c\omega^2h^4}{EI_c}, \quad c = \frac{k_b l_t^2 c_d i}{h\sqrt{m_c EI_c(k_b + \omega c_d i)}} \tag{7}$$

ω in Equation 7 is the circular frequency of system with damper, (It was assumed with frequency of corresponding system without damper here for calculation.) Equation 6 can be solved by iteration when parameter α and c are given. The solution $\{\lambda\} = \{\lambda_1, \lambda_2, \ldots, \lambda_n\}$ of Equation 6 is called the complex eigenvalue vector, and for the i^{th} mode's eigenvalue λ_i, the mode damping ratio ξ_i is calculated by Equation 8, referring to Equation 7 for the dimensionless parameter λ. By substituting λ_i into Equation 3 the shape of the i^{th} mode can also be obtained. Note that the continuous deformation curve produced by Equation 3 needs to be discretized at each floor when conducting mode superposition in latter sections:

$$\xi_j = -\mathrm{Re}(i\lambda_j{}^2)/|\,i\lambda_j{}^2\,| \tag{8}$$

Solving the equivalent continuous cantilever model in Figure 1 with this approach is called the complex eigenvalue analysis method (CEA) hereafter.

COMPARISON ANALYSIS OF MBM MODELS AND CEA MODELS

MBM MODELS AND MODE SUPERPOSITION METHOD

Planar MBM models were constructed using OpenSees for three different outrigger frame buildings of varying heights with RC shear walls and perimeter frames. These are labeled according to the number of stories as the 16F model, 32F model, and 64F model and are shown in Figure 2. A parametric study was then conducted, varying the damped outrigger floor location and damper sizes and is summarized in Table 1. Seismic ground motions used for the time history analysis include BCJ-L2 (Japanese artificial Level 2 wave), El Centro, Hachinohe, JMA Kobe, and Taft, the last four waves were spectrally matched to fit the Level 2 (approximately 500-year event) design response spectrum of the Japanese building code. The peak lateral displacements and story drifts of each model were recorded to evaluate the effects of outrigger location and damper size. All structural members were assumed to remain elastic, and a conventional rigid outrigger was used as a control, modeled with an infinitely large damper as shown in Table 1. The normalized parameters of outrigger stiffness S_{tr} and damping R_{at} will be explained later.

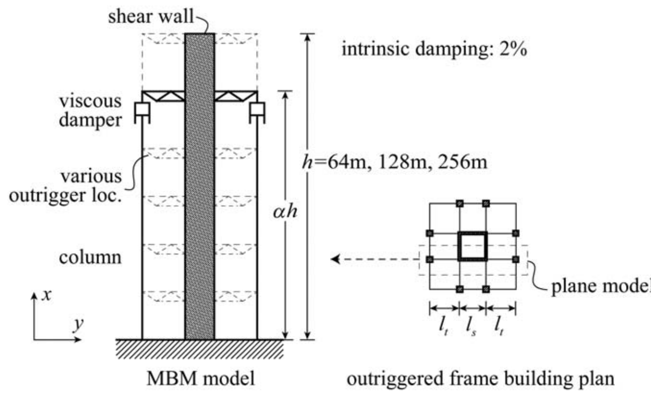

Figure 2. Schematic for the MBM model and outrigger frame building plan.

Mode responses of peak lateral displacement and story drift were combined using the SRSS method and mode damping ratio ξ_i, and the complex mode shapes then calculated from the CEA models.

BASIC STRUCTURAL PARAMETERS

Mode Shapes

Figure 3 shows the first four mode shapes of the 32F CEA models for the case of the outrigger located at the 19th story. The changes due to damper size of the fourth mode shape are listed in Table 1. $\mathrm{Re}(\varphi_j)$ and $\mathrm{Im}(\varphi_j)$ represent the real and imaginary part of j^{th} mode shape, which is complex due to the non-proportional damping provided by the damped-outrigger. The imaginary component is affected by damping and is generally less than the contribution of the real portion of the mode shape. However, for highly damped structures, the relative contribution increases. Furthermore, the bending resistance of the damped outrigger causes a discontinuity of curvature in the imaginary mode shape, which becomes more pronounced in the overall mode shape as the damping and hence relative contribution of

Table 1. Basic information about three types of MBM models

Model series	Height	Period		Damper sizes (kN · sec/mm)	Outrigger loc. (Floor no.)	S_{tr}	R_{at}
16F	64 m	1st	2.0 s	5, 10, 15, 35, 55, 75, 125, ∞	3, 6, 8, 11, 14, 16	1.01	0.15–3.85
		2nd	0.35 s				
32F	128 m	1st	4.2 s	7.5, 15, 35, 55, 75, 125, 175, ∞	3, 6, 13, 19, 26, 32	0.46	0.15–3.57
		2nd	0.6 s				
64F	256 m	1st	7.1 s	15, 35, 55, 75, 125, 175, 225, ∞	6, 12, 18, 24, 30, 36, 42, 48, 54, 60	0.22	0.22–3.23
		2nd	1.1 s				

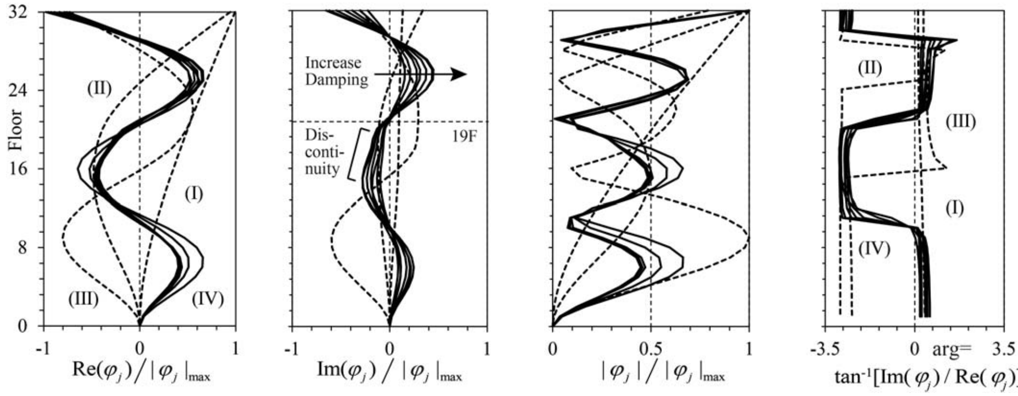

Figure 3. First four mode shapes for 32F models. Outrigger location = 19F.

the imaginary component increases. $|\varphi_j|$ and $|\varphi_j|_{\max}$ represent the mode shape and maximum amplitude, and $\arg = \arctan[\mathrm{Im}(\varphi_j)/\mathrm{Re}(\varphi_j)]$ stands for the phase difference between the real and imaginary components. The mode shapes were calculated using Equations 3–8. Also, the phase angle shown in Figure 3 is equal to either 0 or $-\pi$, and inverts at the mode shape anti-nodes, which suggests geometrical similarity between the real and imaginary components.

Natural Periods and Damping Ratios

Figure 4 shows how the first two natural periods change with outrigger location. MBM models results give several values because of being obtained from the response against different seismic inputs. Generally, the change in period and damping follows a similar trend, and the CEA model can provide a good estimate for both the first- and second modes' periods.

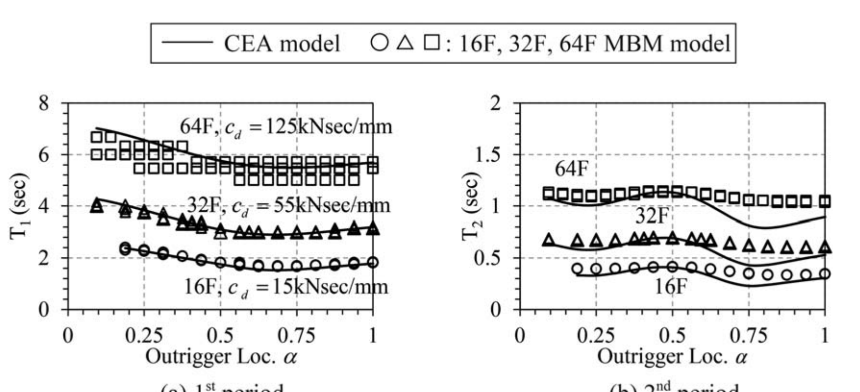

Figure 4. First two modes' periods in 16F, 32F, and 64F models; MBM models' periods were obtained from each input seismic wave. (damper size fixed).

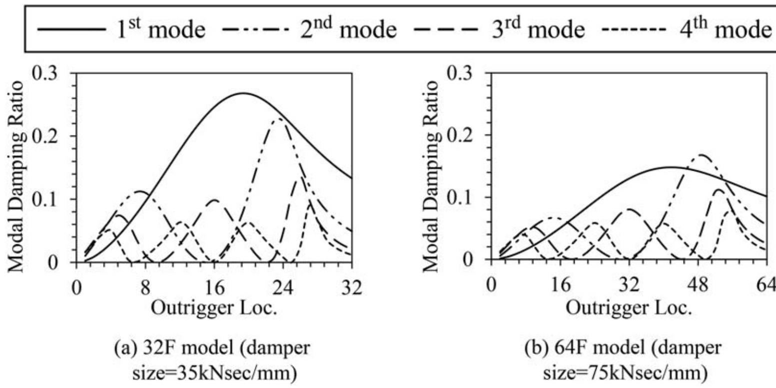

Figure 5. First four mode damping ratios varying with outrigger locations of 32F and 64F CEA models.

Figure 5 shows the variation of the first four mode damping ratios with outrigger location for the 32F and 64F CEA models, assuming a fixed damper size and damping calculated using Equation 8. The achieved damping is strongly correlated to mode shape, with locations corresponding to a mode shape's anti-nodes producing no relative vertical displacement and so resulting in no damping for that mode.

For the MBM model, damping can be calculated by the half-power method. Figure 6 shows the damping ratio as outrigger location is varied. The predicted damping was accurate for the first mode, but the CEA modes tended to overestimate the higher mode damping. This is because of higher mode shape error of CEA model in lower structures. However, given first-mode component is dominant as discussed later, the effects to the response, the optimal outrigger location and damper size is limited.

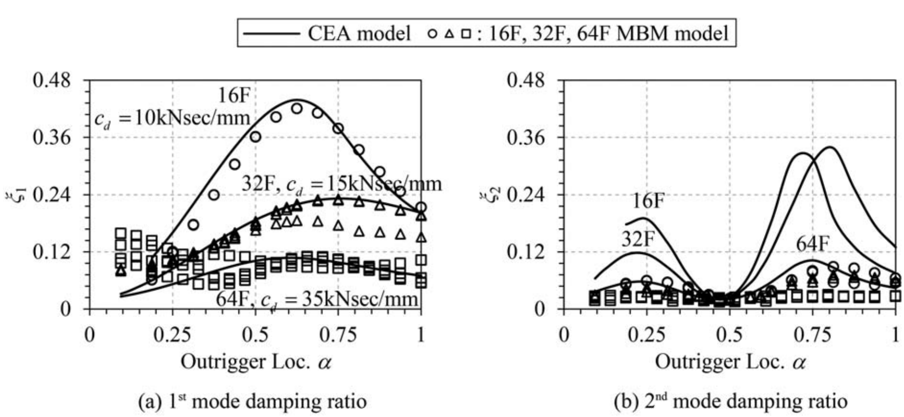

Figure 6. First two mode damping ratios in 16F, 32F, and 64F models (damper size fixed).

Comparing Figure 6 with Figure 4, the period changes little with outrigger location and damper size, while the change in damping is significant. Therefore, the effect of damping is more effective than the period shift effect in reducing the structural response.

SEISMIC RESPONSES COMPARISON BETWEEN MBM AND CEA MODELS

Peak Lateral Displacement and Story Drift

Figure 7 and Figure 8 compare the peak lateral displacement and story drift calculated for a typical case using the MBM and CEA models. As a baseline, the response of a conventional outrigger ($c_d = \infty$) MBM model is also shown. In the story drift in Figure 7, a large discontinuity of curvature in story drift is observed at the outrigger floor of the conventional model, indicating that significant energy is being transferred to other floors. However, the damped-outrigger does not feature this discontinuity and mitigates the overall response as the primary energy dissipation member.

Figure 8a shows that, in all three cases, the CEA and MBM models produced similar results although some bias are observed because of higher mode effects. This figure also reveals that there were no obvious differences in accuracy between the 16F, 32F, and 64F CEA models. Figure 8a also shows that the lateral displacement and story drift are reduced when using a damped-outrigger in comparison with a conventional outrigger ($c_d = \infty$, solid icon).

Peak lateral displacement and story drift obtained for the first mode was also compared with the MBM model results, as shown in Figure 8b. Generally, calculating story drift using only the first mode slightly shifts to underestimate sides in the seismic response and increases errors by 10%, as this neglects the contribution of higher modes. However, their range of varieties is not largely changed from those with using the four modes, which means the first mode is still dominant for the response.

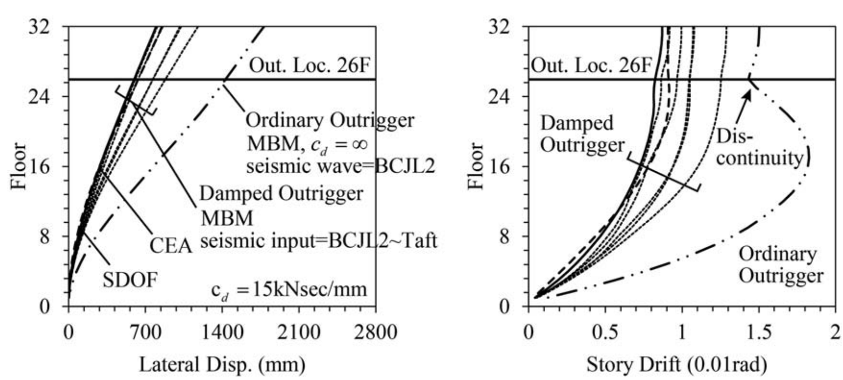

Figure 7. Comparison of peak lateral displacement and story drift of SDOF, CEA, and MBM models.

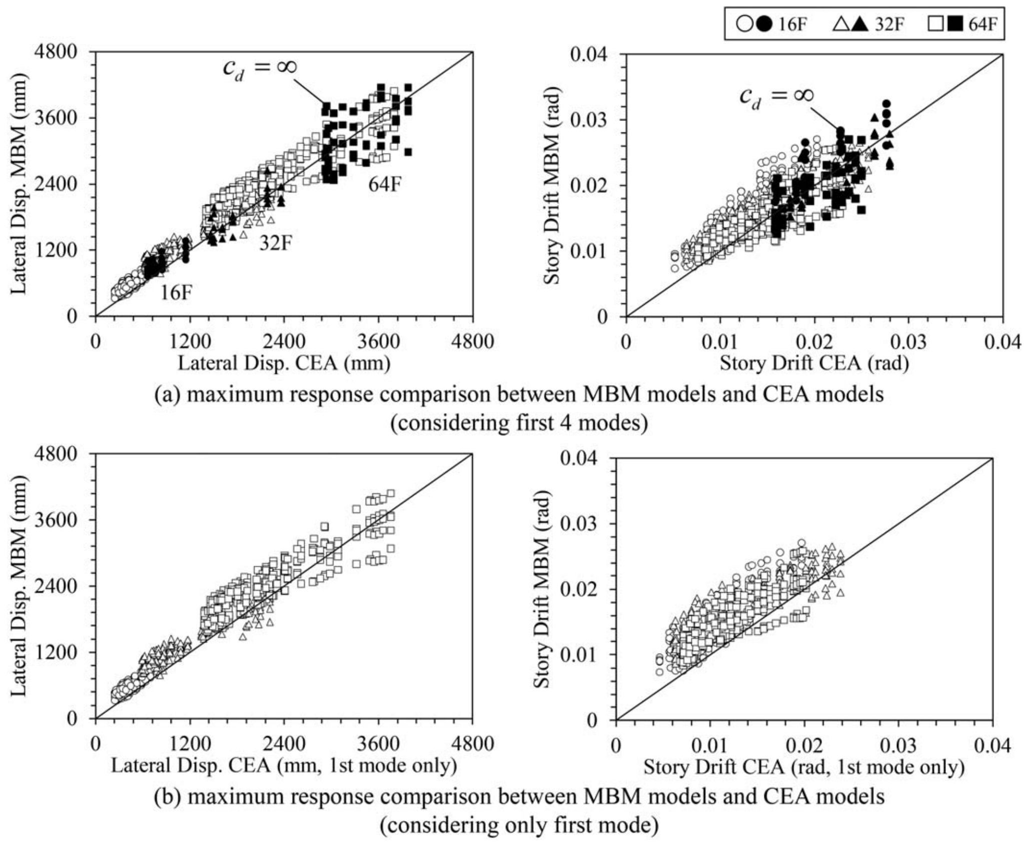

Figure 8. Maximum seismic responses comparison.

Influence of Outrigger Location and Damper Size on Seismic Response

Figure 9 and Figure 10 show the effect of outrigger location and damper size on the total displacement. The solid lines represent the CEA models (combining the first four modes) and the dash lines the MBM models. The MBM and CEA models have reasonably good agreement at each building height.

As the outrigger is moved up in the building, the seismic response first decreases, reaches a minimum, and the increases as shown in Figure 9. The outrigger locations achieving the smallest lateral displacement are between mid-height and the top floor in all cases. The convex shape of the response curves suggests that there is an optimal outrigger location and damper size that can achieve the best performance. A method for determining this optimal configuration is of great practical interest and will be the focus of later sections. The influence of outrigger location and damper size on story drift is similar as lateral displacement.

While the complex eigenvalue analysis (CEA) is approximate, solving the transcendental equations in Equation 6) is difficult and this limits the method's utility in practical use.

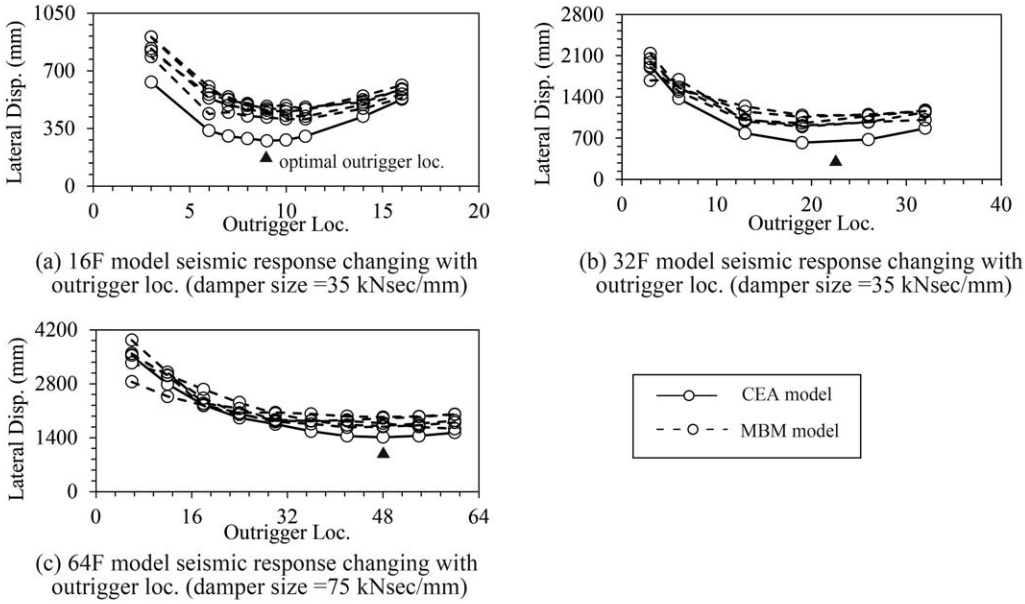

Figure 9. Outrigger location's influence on maximum seismic responses in 16F, 32F, and 64F models.

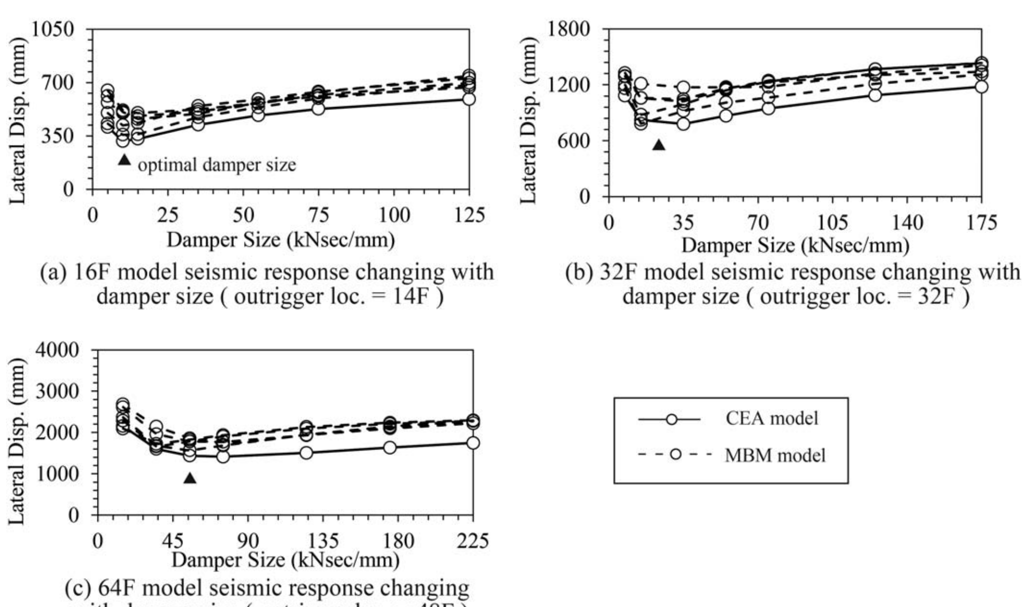

Figure 10. Damper size's influence on maximum seismic responses in 16F, 32F, and 64F models.

Also noting the dominance of the first mode, critical factors in determining the single-damped-outrigger response are the (1) first-mode shape, (2) first-mode damping ratio, and (3) first-mode period. A simplified method derived from the principle of virtual work using a SDOF model which can properly calculate the mentioned three factors is introduced in the following section.

SIMPLIFIED RESPONSES EVALUATION AND OPTIMAL DESIGN METHOD

SDOF MODEL

An approximate response evaluation and optimal design method is developed based on the principle of virtual work and the assumed displacement curve shown in Figure 11. $\tilde{Y}_1$ is the displacement below the outrigger, denoted by segment AB, and $\tilde{Y}_2$ the displacement above the outrigger, denoted by segment BC. $F_{seis.}$ is the virtual seismic force applied at the top of the building, and $M_{seis.}$ is the seismic moment generated at the outrigger location. Other parameters are defined in Figure 1. This simplified model is referred to as the single-degree-of-freedom (SDOF) model hereafter.

The physical displacement curve is assumed to be $y(x,t) = Y(x)q(t)$. In free vibration, the work done by inertia force (δW_m) and internal force (δW_i) under a virtual displacement increment δy should be the same, so that after some simple manipulation, the equation of motion for the equivalent SDOF system is:

$$\bar{M}\ddot{q} + \bar{K}q = 0 \tag{9}$$

where $\bar{M}$ and $\bar{K}$ are the equivalent mass and complex stiffness:

$$\bar{M} = m\int_0^h Y^2(x)dx, \quad \bar{K} = EI_c\int_0^h Y''(x)^2dx + k_r Y'(\alpha h)^2 \tag{10}$$

The equivalent circular frequency $\bar{\omega}$ can then be expressed as:

$$\bar{\omega}^2 = \frac{\bar{K}}{\bar{M}}, \quad i\bar{\omega} = -\bar{\xi}\tilde{\omega} + i\sqrt{1-\bar{\xi}^2}\tilde{\omega} \tag{11}$$

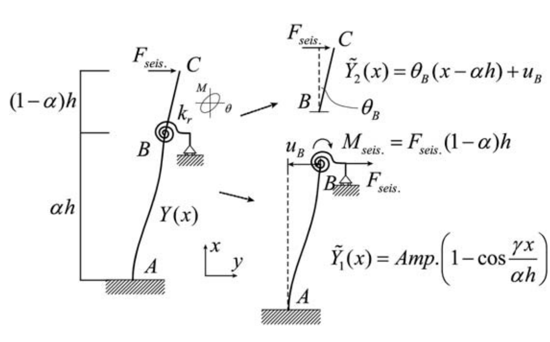

Figure 11. Simplified SDOF model and assumed displacement curve.

where $\tilde{\omega}$ is the non-damped circular frequency. As a result, the damped system's circular frequency ω_D, period T_D and damping ratio $\bar{\xi}$ can be expressed as:

$$\omega_D = \mathrm{Im}(i\bar{\omega}) = \sqrt{1-\bar{\xi}^2}\tilde{\omega}, \quad T_D = \frac{2\pi}{\omega_D}, \quad \bar{\xi} = \frac{-\mathrm{Re}(i\bar{\omega})}{|i\bar{\omega}|} \tag{12}$$

Displacement Curve

The displacement curve was obtained by assuming a concentrated seismic force $F_{seis.}$ is applied at the top floor. Segment AB in Figure 11 is modeled as a cantilever with a tip rotational spring, and subjected to $F_{seis.}$ and $M_{seis.}$. The ratio of lateral displacement to rotation is given by Equation 13 (online Appendix C), neglecting shear deformation:

$$\psi_0 = \frac{u_B}{\theta_B \alpha h} = \frac{3-\alpha}{6-3\alpha} + \frac{K_r}{6EI_c} \cdot \frac{\alpha^2}{2-\alpha} \cdot h \tag{13}$$

where equivalent linear rotational stiffness $K_r = l_t^2 K$ (note difference to k_r). The equivalent vertical stiffness K is defined by the overall bending stiffness of the outrigger truss, perimeter columns and damper on the RC core, and can be expressed as:

$$K^{-1} = (2k_b)^{-1} + (2c_d\omega_D)^{-1}, \quad {k_b}^{-1} = {k_t}^{-1} + \left(\frac{k_c}{\alpha}\right)^{-1} \tag{14}$$

Segment AB's displacement curve is assumed to be sinusoidal and can be expressed as Equation 15, considering boundary conditions:

$$\tilde{Y}_1(x) = Amp.\left(1 - \cos\frac{\gamma x}{\alpha h}\right), \quad \text{subject to} \begin{cases} 0 \le x \le \alpha h \\ \cos\gamma + \psi_0\gamma\sin\gamma - 1 = 0,\ 0 < \gamma < \pi \end{cases} \tag{15}$$

where $Amp.$ represents the first-mode shape amplitude. The geometric parameter γ is a function of the lateral displacement to rotation ratio ψ_0.

The displacement curve for segment BC is taken as an approximately linear function:

$$\tilde{Y}_2(x) = \tilde{Y}_1(\alpha h)' \cdot (x - \alpha h) + \tilde{Y}_1(\alpha h), \quad \alpha h \le x \le h \tag{16}$$

The displacement curve has a much simpler form when compared with the general solution given in Equation 3.

As a result the first-mode equivalent damping ratio is given by:

$$\bar{\xi}(\alpha, c_d) = \frac{1}{\sqrt{2f(\alpha,c_d)^2 + 2\sqrt{f(\alpha,c_d)^4 + f(\alpha,c_d)^2} + 2}} \tag{17}$$

where:

$$f(\alpha, c_d) = \frac{3EI_c}{l_t^2 h k_b} \cdot \left[\frac{k_b}{c_d\omega_D} + \left(\frac{k_b}{c_d\omega_D}\right)^{-1}\right]\frac{1}{\alpha} \times \left(\frac{\gamma^2}{12\sin^2\gamma} + \frac{\gamma\sin 2\gamma}{24\sin^2\gamma}\right) + \left(\frac{k_b}{c_d\omega_D}\right)^{-1} \tag{18}$$

In Equations 17 and 18, the only unknown variables are the outrigger location α and damper size c_d, as the RC core bending stiffness EI_c and column-outrigger truss stiffness k_b are reasonably assumed to be constant here rather than a function of outrigger location α, which will make following analysis simpler. As Equation 18 is used to predict the damping ratio $\bar{\xi}$, but is a function of the damped frequency ω_D, iteration can be avoided by substituting the non-damped first-mode frequency $\tilde{\omega}_1$, and refer to the approximate function as damping function $\bar{f}(\alpha, c_d)$.

MODE SHAPE, DAMPING RATIO AND NATURAL PERIOD OF SDOF MODEL

Mode Shapes

Using the displacement curve given by Equation 15 and Equation 16, the mode shape of the SDOF model with different outrigger locations and damper sizes can be obtained and compared with the first mode of the CEA model, given by Equation 3. Figure 12 shows the change with increasing damper size. Generally, the rotation constraining effect of the damped-outrigger is more obvious in the CEA model, especially when damper size is

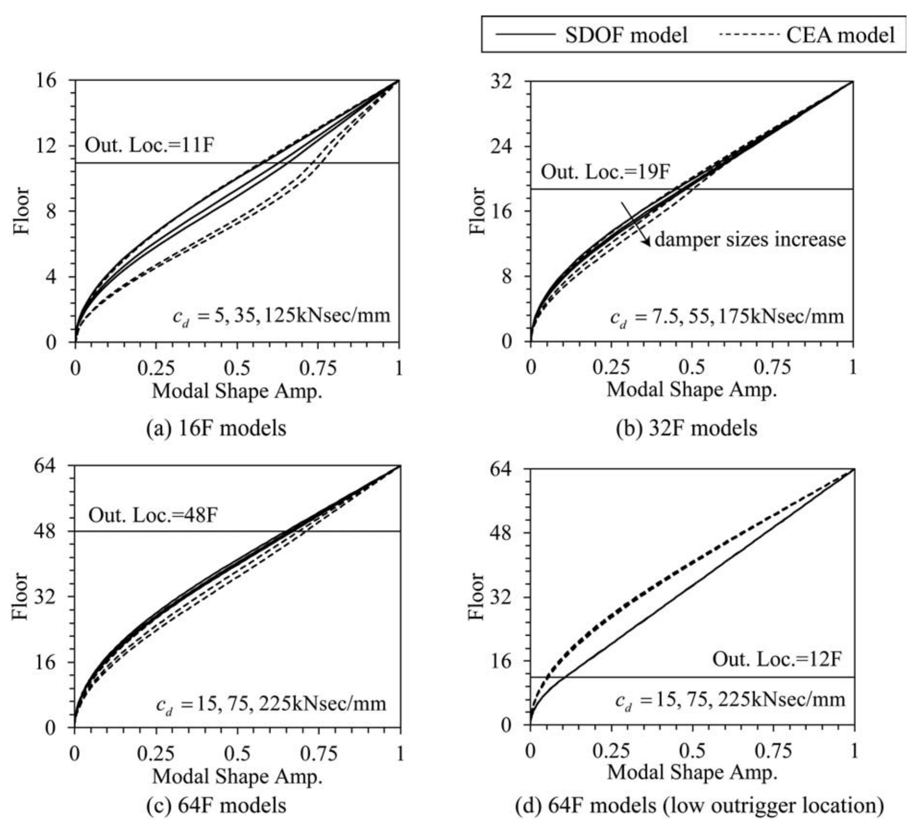

Figure 12. First-mode shape comparison of SDOF model and CEA model.

large in 16F model, but the SDOF is still a good representation for outrigger locations above mid-height and for reasonably sized dampers in 32F and 64F models.

Damping Ratios

The SDOF model damping ratios can be calculated using Equation 12, and in Figure 13 are compared with the CEA model, given by Equation 8. Good agreement was achieved for the 32F and 64F models, but the SDOF 16F model deviated substantially. This is because the imaginary components of the mode displacement curves include the damping effect, and so at the damped-outrigger floor a discontinuity is observed. This discontinuity is more significant in the CEA than SDOF mode shape.

Natural Periods

The fundamental frequencies of the SDOF models can be obtained from the damping ratios and corresponding non-damped frequencies in Equation 12. The first-mode periods of the CEA models were compared in Figure 13b. When the outrigger location is low, the SDOF model appears to underestimate the first-mode period. This is because the displacement curve is unable to accurately simulate the first-mode shape when the outrigger is located close to the base floor, as shown in Figure 12(d). To ensure that the fundamental period is accurately estimated, use of the SDOF model should be limited to buildings whose outrigger is located above mid-height.

SEISMIC RESPONSES COMPARISON WITH MBM AND CEA MODELS

Figure 14 summarizes the maximum responses of the SDOF, MBM and CEA models, similar to Figure 8. The outrigger location is limited to $\alpha > 0.5$. In Figure 14a, the SDOF and CEA models both slightly underestimate the peak lateral displacement, but are otherwise in good agreement with each other. Figure 14b compares the story drift, showing that the SDOF

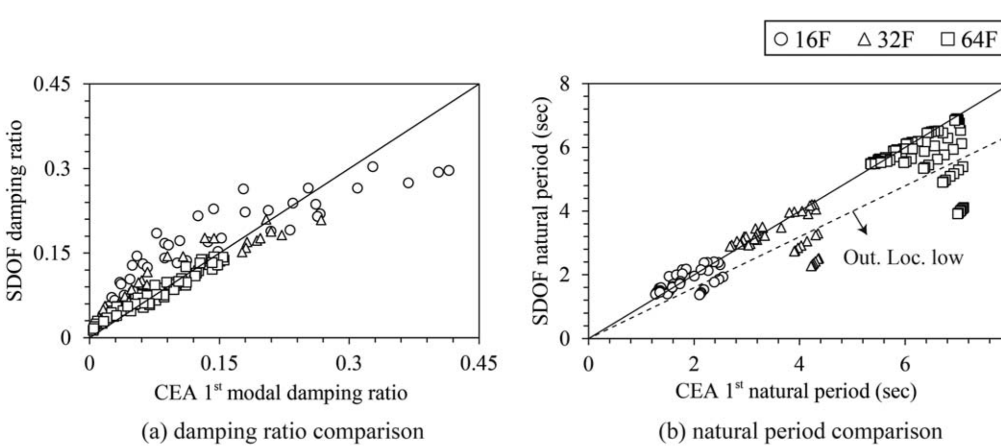

Figure 13. Damping ratio and period comparison of SDOF models and CEA models.

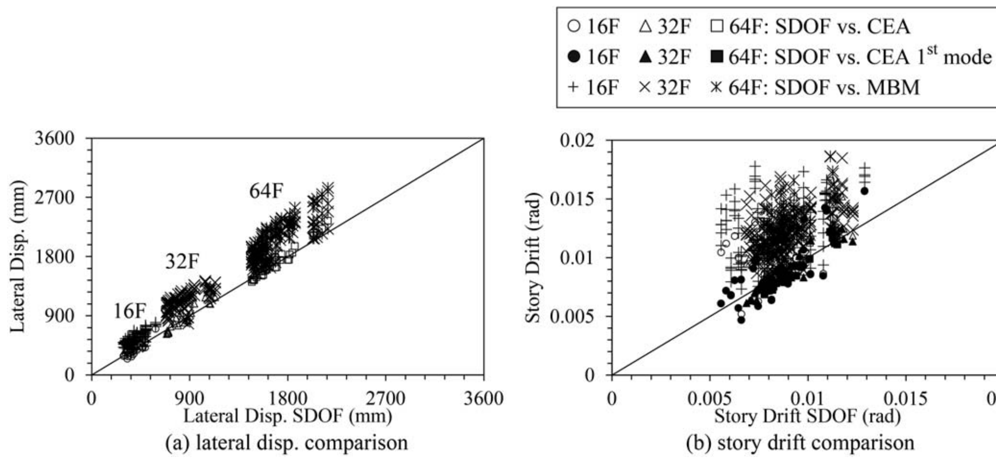

Figure 14. Maximum seismic response comparison of SDOF, MBM, and CEA models ($\alpha > 0.5$).

underestimates the drift relative to the CEA and MBM models. Generally, the prediction of peak lateral displacement is much better than that of story drift, because in story drift response, higher modes' components possess larger portion of total response value than in lateral displacement. So the SDOF model is applicable for evaluating maximum lateral displacement with safety factors of around 30%, while the CEA model is more suitable for evaluating story drifts.

OPTIMAL OUTRIGGER LOCATION AND DAMPER SIZE OF SDOF MODEL

As previously discussed, the damping ratio $\bar{\xi}$ is more critical than the period shift effect in controlling the dynamic response. Also, the optimal outrigger location α and damper size c_d often correspond to maximum first-mode damping ratio, as shown in Figure 6a and Figure 9. Therefore, the optimal outrigger location and damper size to achieve the maximum mode damping ratio $\bar{\xi}$ are defined as α_{opt} or $c_{d,opt}$ using SDOF model.

The optimization problem of maximizing the damping ratio $\bar{\xi}$ in Equation 17 is equivalent to minimizing the damping function $\bar{f}(\alpha, c_d)$. The damping function $\bar{f}(\alpha, c_d)$ is composed of three dimensionless parameters summarized as follows:

$S_{tr} = \frac{l_t^2 h k_b}{3EI_c}$: outrigger stiffness parameter (larger with stiffer outrigger);
$R_{at} = \frac{c_d \tilde{\omega}_1}{k_b}$: damping parameter (larger with higher damping);
α : outrigger location

The values of S_{tr} and R_{at} for the 16F, 32F and 64F MBM models are summarized in Table 1. When the building increases in height, the outrigger stiffness parameter S_{tr} decreases and for the example models varies from 0.22 to 1.01. For actual buildings less than 200 m in height (64F model), S_{tr} would be expected to vary between $0.2 \le S_{tr} \le 2$.

The damping parameter R_{at} is always larger than 0.1, with $R_{at} \le 0.1$ corresponding to ineffectively small damping (e.g., $c_d = 5\,\mathrm{kNsec/mm}$ for a 32F model or $c_d = 3\,\mathrm{kNsec/mm}$ for a 16F model). In Figure 10, the optimal damper size was always found within the range of damper sizes considered, and so the optimal value would be expected to correspond to $R_{at} \ge 0.1$.

In Figure 9, the optimal outrigger locations α_{opt} are above the mid-height for all cases. Therefore, we assume that α varies between $0.4 \le \alpha \le 1$ to determine the optimal outrigger location. Using the least square function fitting when $\alpha \in [0.4, 1]$, optimal outrigger location α_{opt} can be approximately expressed by:

$$\alpha_{opt} = \frac{3.278 S_{tr}^2 R_{at}^2 + 0.751 S_{tr}(1 + R_{at}) R_{at} + 0.573(1 + R_{at})^2}{6.75 S_{tr}^2 R_{at}^2 + 1.805 S_{tr}(1 + R_{at}) R_{at} + 0.625(1 + R_{at})^2} \tag{19}$$

Here R_{at} (damper size) is considered to be a constant. Substituting the optimal outrigger location expressed in Equation 19 into the damping ratio $\bar{\xi}$ given in Equation 17, the maximum damping ratio of SDOF models can be obtained.

Similarly, the optimal stiffness ratio for R_{at} when S_{tr} and α are fixed can be approximately expressed by Equation 20, and the optimal damper size obtained by referring to previous equations.

$$R_{at,opt} = \sqrt{\frac{0.199\alpha^2 - 0.59\alpha + 0.606}{2.009\alpha^4 S_{tr}^2 + S_{tr}\alpha(\alpha - 2)^2}}, \quad c_{d,opt} = \frac{k_b R_{at,opt}}{\omega_1} \tag{20}$$

Responses Comparison Between Optimized and Non-Optimized Models

The proposed method for determining the optimal outrigger location and damper size by maximizing the damping ratio of the SDOF model was verified by applying Equation 19 and Equation 20 to the MBM models listed in Table 1, and the results are summarized as follows.

Figure 15 compares the seismic responses of the MBM models with optimized outrigger locations calculated from Equation 19 and the original models. For the 32F and 64F models, the optimized models generally achieved the smallest lateral displacement and story drift. Generally, increasing the damper size for the optimized model led to worse performance, because when damper size increased over the optimal size, the stiffness of equivalent rotational spring increases and approaches to ordinary outrigger system whose equivalent damping ratio decreases. In all cases, the optimal outrigger locations were above 40% of the building height, $0.4 \le \alpha \le 1$.

Using Equation 20, the damper sizes c_d of the models listed in Table 1 are set to the optimal damper sizes $c_{d,opt}$, given an outrigger location α. The seismic response comparison of various outrigger locations is shown in Figure 16. Generally, the optimized damper size is able to capture the minimum response from the original non-optimized models. Hence the proposed optimal equations using SDOF models are considered to be valid for

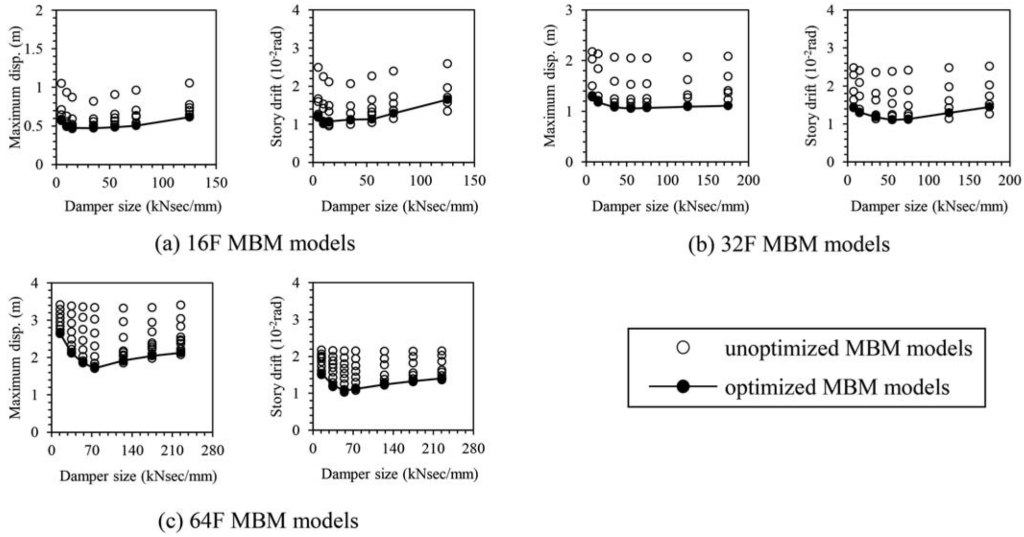

Figure 15. Seismic responses of 16F, 32F, and 64F MBM models with optimal outrigger location by Equation 19. Input seismic wave: BCJ-L2.

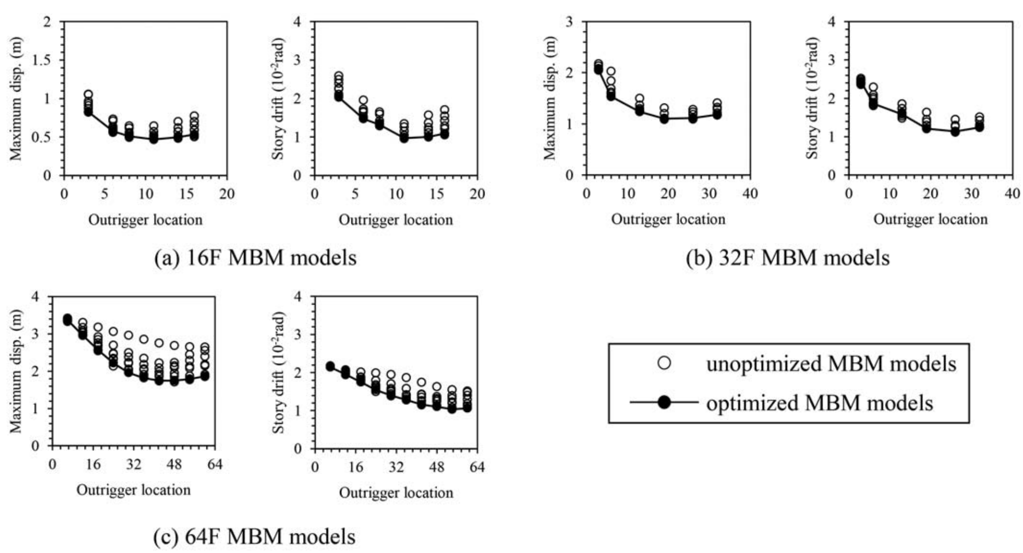

Figure 16. Seismic responses of 16F, 32F, and 64F MBM models with optimal damper size by Equation 20. Input seismic wave: BCJ-L2.

determining the optimal outrigger location and damper size even the evaluated response values are approximate. These equations are also available for multipurpose optimization as shown in Figure 17, by iterative process.

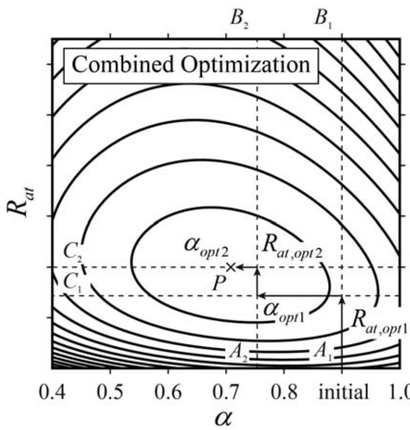

Figure 17. Combined optimization.

PERFORMANCE CURVE AND DESIGN METHOD BASED ON SDOF MODEL

The SDOF model is sufficient to estimate the rough seismic response of the single-damped-outrigger system, and to optimize the outrigger location or damper size. In this section, the relationship between natural period, damping ratio $\bar{\xi}$, outrigger location α, and stiffness ratio R_{at} is further summarized in step by step procedures, followed by a performance curve proposal. This graphical method enables the engineer to easily evaluate the seismic response mitigation effect for a given α and R_{at}.

As previously discussed, the SDOF model's accuracy is better for moderating damping ratios ($\xi \leq 0.2$), such as those achieved in the 32F and 64F models, and when the outrigger location α satisfies $0.4 \leq \alpha \leq 1$. As the period is not as sensitive to changes in the outrigger location α and damper size c_d as the mode damping ratio (Figures 4 to 6), this section will be limited to discussion of effect of varying α and c_d.

Performance curves (JSSI 2005) of the 32F and 64F models are shown in Figure 18. Because both of these models are in the velocity constant region, the displacement and acceleration reduction factor are expressed as:

$$r_d = \frac{S_d(T_D, \xi_{eq})}{S_d(T_f, \xi_0)} = D_h \cdot \frac{T_D}{T_f}, \quad r_a = \frac{S_a(T_D, \xi_{eq})}{S_a(T_f, \xi_0)} = D_h \cdot \frac{T_f}{T_D} \tag{21}$$

where:

$$D_h = \sqrt{\frac{1 + 75\xi_0}{1 + 75\xi_{eq}}}, \quad \xi_0 = 0.05, \quad \xi_{eq} = \bar{\xi} + \xi_0 \tag{22}$$

D_h is a parameter reflecting damping's mitigation effect on seismic responses, and T_D is natural period of system with damper, while T_f without damper (only frame). In Figure 18a and 18b, minimum values of r_d and r_a are obtained at almost the same point with $R_{at} \approx 0.6$

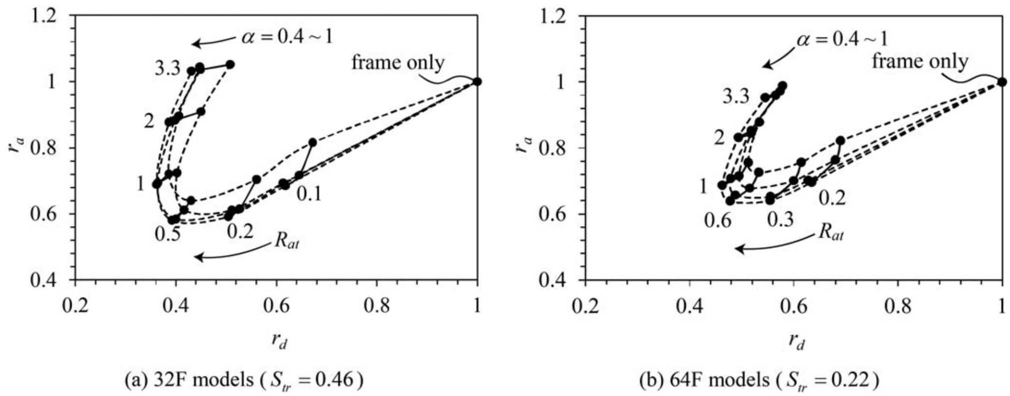

Figure 18. Performance curve of 32F and 64F models.

($c_d = 30\,\text{kNsec/mm}$ for 32F model, $c_d = 60\,\text{kNsec/mm}$ for 64F model) and $\alpha \approx 0.8$. The optimal design method proposed above suggests that the displacement and acceleration response can be reduced to 50% and 60%, respectively, of the non-damped model. Moreover, an excessively large damper is inefficient in displacement reduction and will magnify the acceleration response, which suggests that a conventional outrigger system ($c_d = \infty$) will have a relatively poor performance.

The design process based on the SDOF model is outlined in Figure 19. First, the main structure (RC core) is sized and the outrigger-column stiffness (k_b) determined, resulting in $S_{tr} = const$. The structural response is formulated as a function of outrigger location α and damper size c_d, as expressed in the damping function $\bar{f}$. Next, confirm that the parameters, α, S_{tr} and R_{at}, are within the applicable range for the proposed fitting functions and select the appropriate design target. Use Equation 19 to optimize the outrigger location holding the damper size constant, otherwise optimize the damper size for a given outrigger location using Equation 20. After α (or α_{opt}), S_{tr} and R_{at} (or $R_{at,opt}$) are determined, the period

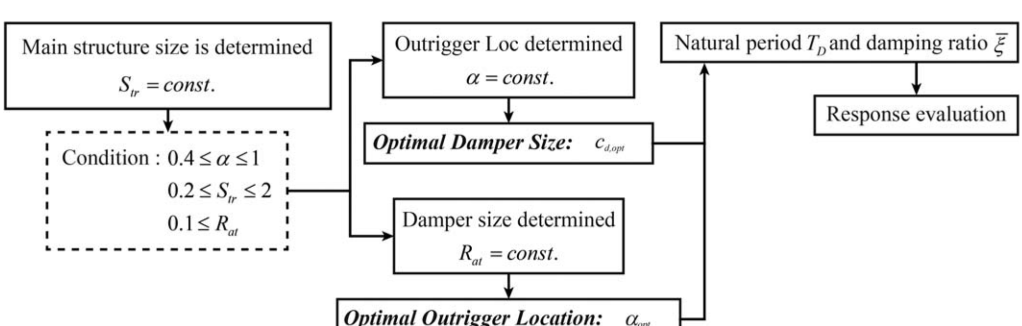

Figure 19. Optimal design process for determining outrigger location and damper size.

T_D and damping ratio $\bar{\xi}$ can be evaluated using Equation 12, and a design response spectrum used to determine the structural response, such as peak lateral displacement and story drift with some safety factors.

CONCLUSIONS

In this paper, complex eigenvalue analysis (CEA) was used to obtain the seismic peak lateral displacement and story drift of a single-damped-outrigger system, including higher mode effects. A simplified SDOF model based the first-mode shape and virtual work was then proposed and its accuracies verified through a comparison study. The optimal outrigger location and damper size can be determined using newly proposed stiffness and damping indexes, S_{tr} and R_{at}, respectively. In summary:

1. The CEA model is able to evaluate the single-damped-outrigger system's dynamic response, including peak lateral displacement and story drift. In this study, good agreement was achieved for the taller buildings (≥32 stories). The mode shape, damping and period of the first-mode are the three most important factors affecting the structural response. The damping ratio is the most sensitive to the outrigger location and damper size, and thus it is most capable of influencing the structural response.
2. There are optimal values of outrigger location α_{opt} and damper size $c_{d,opt}$ to minimize the structural dynamic response. The optimal values of α_{opt} and $c_{d,opt}$ increase with building height. The optimal outrigger location typically falls between $0.5 < \alpha_{opt} < 0.8$, and the optimal damping parameter (which determines the damper size) between $0.5 < R_{at} < 1$. However, the achievable damping ratio reduces with building height as well as the achievable response reduction effect.
3. A simplified SDOF model derived from the principle of virtual work is confirmed to be valid in evaluating the response of the single-damped-outrigger system when the outrigger location $\alpha \geq 0.4$ and number of stories is ≥32.
4. The optimal outrigger location α_{opt} and damper size $c_{d,opt}$ can be evaluated based on the simplified SDOF model using the proposed outrigger stiffness index S_{tr} and damper size index R_{at}, by assuming α_{opt} and $c_{d,opt}$ are parameters by which the first-mode's maximum damping ratio is achieved. Performance curves for evaluating the response reduction effect are presented.

These studies are limited in scope to the single-damped-outrigger system. However, following studies have already confirmed that the same approach is applicable for multileveled damped-outrigger-systems, which will be reported in the near future.

ACKNOWLEDGMENTS

The authors would like to express deep thanks to Mr. Ben Sitler and Dr. Matsui for their thoughtful advises and reviews for organizing this study.

APPENDIXES

Please refer to the online version of this manuscript to access the supplementary material provided in the appendixes.

REFERENCES

Ali, M. M., and Moon, K. S., 2007. Structural developments in tall buildings: current trends and future prospects, *Architectural Science Review* **50**, 205–223.

Architectural Institute of Japan (AIJ), 2000. *Damping in Buildings*, Maruzen Publishing Co., Tokyo, 65–122.

Chen, Z., and Wang, Z., 2009. A novel passive energy dissipation system for frame-core tube structure, in *Proceedings, The 7th Asia-Pacific Conference on Wind Engineering*, Taipei, 6 pp.

Chen, Y., McFarland, D. M., Wang, Z., Spencer, Jr., B. F., and Bergman, L. A., 2010. Analysis of tall buildings with damped outriggers, *Journal of Structural Engineering* **136**, 1435–1443.

Fu, Y., and Kasai, K., 1998. Comparative study of frames using viscoelastic and viscous dampers, *Journal of Structural Engineering* **124**, 513–522.

Japan Society of Seismic Isolation (JSSI), 2005. *Manual for Design and Construction of Passively-Controlled Buildings*, 2nd edition, Daioh Co., Ltd., Tokyo, 43–53.

Jeremiah, C., 2006. Application of Damping in High-Rise Buildings, M.S. Thesis, Massachusetts Institute of Technology, Cambridge, MA.

Laura, P. A. A., Susemihl, E. A., Pombo, J. L., Luisoni, L. E., and Gelos, R., 1977. On the dynamic behavior of structural elements carrying elastically mounted, concentrated masses, *Applied Acoustics* **10**, 121–145.

Mazzoni, S., McKenna, F., Scott, M. H., and Fenves, G. L. 2009. *OpenSees Version 2.0 User Manual*, Pacific Earthquake Engineering Research Center (PEER), University of California, Berkeley, available at http://opensees.berkeley.edu.

Lu, X., Zou, Y., Lu, W., and Zhao, B., 2007. Shaking table model test on Shanghai World Financial Center Tower, *Earthquake Engineering and Structural Dynamics* **36**, 439–457.

Osaki, Y., 1994. *Fundamentals of Seismic Spectral Analysis*, 2nd edition, Kajima Publishing Co., Tokyo, 25–83.

Smith, R. J., and Willford, M. R., 2007. The damped outrigger concept for tall buildings, *Struct. Design Tall Spec. Build.* **16**, 501–517.

Tan, P., Fang, C. J., Tu, W. R., Zhou, F. L., Wang, Y., and Jiang, M., 2012. Experimental study on the outrigger damping system for high-rise building, in *Proceedings, The 15th World Conference on Earthquake Engineering*, Lisbon, 7 pp.

Tan, P., Fang, C. J., and Zhou, F. L., 2014. Dynamic characteristics of a novel damped outrigger system, *Earthquake Engineering and Engineering Vibration* **13**, 293–304.

Viise, J., Ragan, P., and Swanson, J., 2014. BRB and FVD alternatives to conventional steel brace outriggers, in *Proceedings, CTBUH 2014 Shanghai Conference*, Paper No. 691, Shanghai, 9 pp.

Willford, M. R., and Smith, R. J., 2008. Performance based seismic and wind engineering for 60 story twin towers in Manila, in *Proceedings, The 14th World Conference on Earthquake Engineering*, Beijing, 8 pp.

Wu, J.-S., Chen, D.-W., and Chou, H.-M., 1999. On the eigenvalues of a uniform cantilever beam carrying any number of spring-damper-mass systems, *International Journal for Numerical Methods in Engineering* **45**, 1277–1295.

Wu, J.-S., and Chou, H. M., 1998. Free vibration analysis of a cantilever beam carrying any number of elastically mounted point masses with the analytical-and-numerical-combined method, *Journal of Sound and Vibration* **213**, 317–332.

(Received 18 May 2016; accepted 12 January 2017)